A comprehensive study on electrochemical performance of Mn-surface-modified LiNi$_{0.8}$Co$_{0.15}$Al$_{0.05}$O$_2$ synthesized by an in situ oxidizing-coating method

CrossMark

Bin Huang, Xinhai Li*, Zhixing Wang, Huajun Guo, Li Shen, Jiexi Wang

School of Metallurgy and Environment, Central South University, Changsha 410083, China

HIGHLIGHTS

- Mn is uniformly doped at the surface of LiNi$_{0.8}$Co$_{0.15}$Al$_{0.05}$O$_2$ particles.
- The capacity fading under room temperature and high temperature is suppressed.
- The capacity fading under overcharge condition is suppressed.
- The degradation during storage in air is delayed.

ARTICLE INFO

ABSTRACT

The degradation of Ni-rich LiNi$_{0.8}$Co$_{0.15}$Al$_{0.05}$O$_2$ cathode material is successfully suppressed via a facile in situ oxidizing-coating method. KMnO$_4$ is used as not only a Mn source but also an oxidant. X-ray diffraction (XRD) and scanning electron microscope (SEM) results demonstrate that the structure and morphology of the KMnO$_4$-pretreated sample are the same as the pristine one. X-ray photoelectron spectroscopy (XPS) confirms that the valence state of Mn is +4 and the Ni^{3+} ions are partly reduced to Ni^{2+} when the material is doped with Mn^{4+}. Besides, the Mn^{4+} ions are proved to distribute uniformly on the surface of the materials particles through energy dispersive spectrometer (EDS) and EDS elemental mapping. And it is confirmed that the concentration of Ni in the outer layer is reduced by the Mn-surface-modification. From the electrochemical characterizations, it is confirmed that the presence of tetravalent Mn at the surface can suppress the capacity fading during charge–discharge cycles, even under elevated temperature and overcharge conditions, and can prevent the material from deterioration during storage in air.

© 2013 Elsevier B.V. All rights reserved.

1. Introduction

Ni-based layered Li[Ni$_{1-x}$M$_x$]O$_2$ (M = transition metal) have been considered as a very promising candidate for large-scale application such as electric vehicles (EVs), hybrid electric vehicles (HEVs) and plug-in hybrid vehicles (PHEVs) due to its low cost, low toxicity and high energy density [1–4]. However, the chemical instability of Ni^{3+} and Ni^{4+} has been considered as a critical factor to the fast aging rate, thermal instability and poor storage characteristics in air for the Ni-based materials, especially for the highly Ni-contained series (the *x* value is no more than 0.2 in Li[Ni$_{1-x}$M$_x$]O$_2$) [1,2,5–7]. In this Ni-based family, Co and Al co-substituted LiNi$_{0.8}$Co$_{0.15}$Al$_{0.05}$O$_2$ is one of the most applicable materials due to the improved electrochemical properties and thermal stability. Nevertheless, there remain problems unsolved. Some structural and electrochemical analyses of the LiNi$_{0.8}$Co$_{0.15}$Al$_{0.05}$O$_2$ cathode material have revealed that the Ni cations irreversibly migrate from the transition metal layers to the Li slabs and form an electrochemically inactive NiO-like phase during delithiation, resulting in the degradation of the cathode material and impedance rise of the entire cell [8–11]. In addition, confirmed by these investigations, the degradation will begin from the surface of the material particles. Thus, how to improve their cycling performance and increase durability in service or storage is worth studying.

In order to enhance the electrochemical and thermal properties, many strategies were proposed. Substituting other cations in Ni-based materials has been shown to improve the structural stability and suppress the degradation [8,12–14]. Moreover, some other methods are classified as surface protection which falls into two

* Corresponding author. Tel./fax: +86 731 88836633.
E-mail address: xinhaili_csu@126.com (X. Li).

categories: surface coating [15–18] and core–shell structure [19,20]. For the former, some stable oxides, fluorides and phosphates are used to prevent the trace amount of HF from attacking cathode materials; and for the later another structurally stable cathode material acts as a protective shell for the Ni-based core. In addition, the concentration-gradient materials have also shown the attraction due to the relatively stable surface [21–23]. Recently, Cho et al. [24] reported a novel surface pillaring layer protected $LiNi_{0.70}Co_{0.15}Mn_{0.15}O_2$, which was prepared from MnO_2-coated $Ni_{0.70}Co_{0.15}Mn_{0.15}(OH)_2$ precursor. In their study, the surface Mn^{4+} was proved to induce the reduction of Ni^{3+} to Ni^{2+} during the annealing process due to the charge compensation. And a part of the Ni^{2+} simultaneously migrate to Li slabs and form a nanoscaled NiO pillaring layer, which could block the side-reactions between the cathode and electrolyte associated with the structural distortion and capacity fading. And Noh et al. [25] synthesized an interesting concentration-gradient material with a $LiNi_{0.8}Co_{0.2}O_2$ center and a $LiNi_{0.8}Co_{0.01}Mn_{0.19}O_2$ surface. It was confirmed by them that, although the high Ni concentration was maintained from the particle center to the surface, the cycling performance and thermal properties could be significantly improved by tetravalent Mn modifying on the surface.

In this study, we comprehensively investigate the electrochemical properties of a Mn-surface-modified $LiNi_{0.8}Co_{0.15}Al_{0.05}O_2$ which is prepared from a MnO_2-coated $Ni_{0.8}Co_{0.15}Al_{0.05}(OH)_2$ precursor. The precursor is coated by a novel approach in which a uniform MnO_2 layer can be achieved. $KMnO_4$ solution is used in the treating process for providing MnO_2 coating layer based on the redox reaction between MnO_4^- and Ni^{2+}.

2. Experimental

The pristine $Ni_{0.8}Co_{0.15}Al_{0.05}(OH)_2$ precursor was obtained by commercial supply. The in situ oxidizing-coating process was implemented as below. $KMnO_4$ powder was dissolved in deionized water to form a 0.1 mol L^{-1} solution. Subsequently, 10 g $Ni_{0.8}Co_{0.15}Al_{0.05}(OH)_2$ precursor was dispersed in deionized water, followed by dripping 20 mL the as-prepared $KMnO_4$ solution with magnetic stirring. On the surface of the precursor, Ni^{2+} was immediately oxidized into Ni^{3+}, accompanied by the precipitation of MnO_2. As a result, the dark green solid powder was changed into dark brown, and the dripped violet liquid immediately became clear. But the violet could no longer fade within 1 h when about 15 mL $KMnO_4$ solution was dripped in. Then excess 5 mL was added with stirring for 0.5 h. After reaction, the dark brown powder was recovered by filtration, washed three times with deionized water and dried at 110 °C overnight. Finally, the MnO_2-coated $Ni_{0.8}Co_{0.15}Al_{0.05}(OH)_2$ and $LiOH \cdot H_2O$ were thoroughly mixed with a molar ratio of 1:1.05 before being sintered at 750 °C for 15 h under flowing oxygen. For comparison, a pristine sample was obtained by annealing pristine $Ni_{0.8}Co_{0.15}Al_{0.05}(OH)_2$ and $LiOH \cdot H_2O$ with the same molar ratio and sintering process. For convenience, the $KMnO_4$ treated $Ni_{0.8}Co_{0.25}Al_{0.05}(OH)_2$ precursor and the pristine one are labeled as T-precursor and U-precursor; and the materials synthesized from them are labeled as T-NCA and U-NCA respectively.

X-ray diffraction (XRD) patterns were measured using a Rigaku Rint-2000 diffractometer with Cu-Kα radiation (1.54056 Å). The morphologies of the as-prepared samples were observed by a scanning electron microscope (SEM, JEOL, JSM-5612LV). The amount of Mn attached onto the material particles is detected by an inductively coupled plasma optical emission spectrometer (ICP-OES, IRIS Intrepid II XSP). Moreover, X-ray photoelectron spectroscopy (XPS, PHI 5600, Perkin–Elmer) measurements were performed to get information on the surface of the materials.

CR 2025 coin-type cells were assembled with metallic lithium anodes for electrochemistry studies. The positive electrodes were fabricated by casting a slurry consisting of as-prepared sample (80 wt%), Super P carbon black (10 wt%) and poly(vinylidene fluoride) (PVDF) (10 wt%) dispersed in N-methyl-2-pyrrolidone (NMP) onto an aluminum foil with a doctor blade, followed by drying at 120 °C under vacuum for 12 h 1 M $LiPF_6$ in 1:1:1 ethylene carbonate/ethyl methyl carbonate/dimethyl carbonate was used as electrolyte. The cells were assembled in an Ar-filled glove box (Mikrouna) with O_2 and H_2O lower than 0.5 ppm, and cycled galvanostatically between 2.8 and 4.3 V (vs. Li/Li^+) (or between 2.8 and 4.5 V for overcharge behaviors study) at a desired current density.

3. Results and discussion

3.1. Physical characterizations

Fig. 1 shows the XRD patterns of the pristine and $KMnO_4$ treated $Ni_{0.8}Co_{0.15}Al_{0.05}(OH)_2$ (U-precursor and T-precursor). We can see that the diffraction peak positions of the T-precursor fit well with the ones of the U-precursor, indicating no structural change occurred when the precursor was treated by $KMnO_4$. Fig. 2 represents the XRD patterns of U-NCA and T-NCA. As can be seen, the two samples all adopt α-$NaFeO_2$ structure, $R\bar{3}m$ space group. The lattice constants a and c are calculated based on the X-ray diffraction patterns and listed in Table 1, together with the values of c/a and $I_{(003)}/I_{(104)}$ which can reflect the degree of cation mixing in the layered hexagonal structure with a $R\bar{3}m$ space group [24,26]. As indicated by Table 1, the T-NCA sample has slightly lower c/a and $I_{(003)}/I_{(104)}$ values, showing a higher degree of cation mixing in T-NCA, and this is in accord with Cho's report [24]. This cation mixing may result from the surface doping of tetravalent Mn. The valence state of Ni and Mn will be further detected by XPS.

The XPS spectra of Mn $2p_{3/2}$ for T-precursor and T-NCA are shown in Fig. 3. The binding energies of Mn $2p_{3/2}$ in the two samples are both 642.2 eV which indicates the presence of Mn^{4+} at the surface [12]. Fig. 4 shows the XPS of Ni for U-NCA and T-NCA. As seen in Fig. 4a, the Ni $2p_{3/2}$ peak of T-NCA is at 854.1 eV, which is slightly lower than U-NCA (854.5 eV). Fig. 4b and c shows the magnified spectra of Ni $2p_{3/2}$ peaks of U-NCA and T-NCA respectively, together with the results of the semi-quantitative analysis for Ni^{2+} and Ni^{3+} by Avantage software. These results confirm more presence of Ni^{2+} at the surface of T-NCA than U-NCA due to the charge compensation when Mn^{4+} ions are introduced into the surface layer [24].
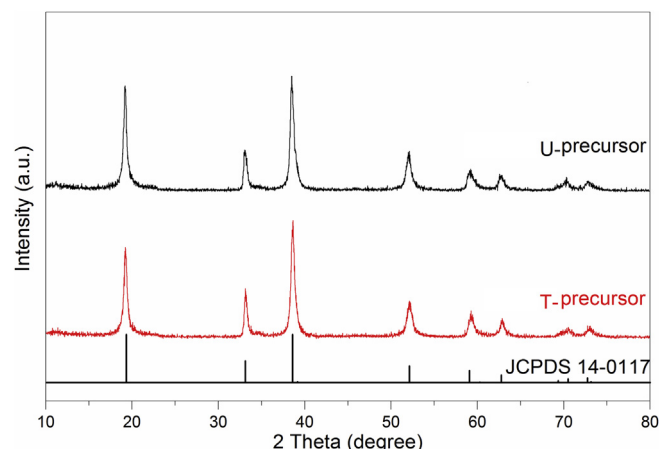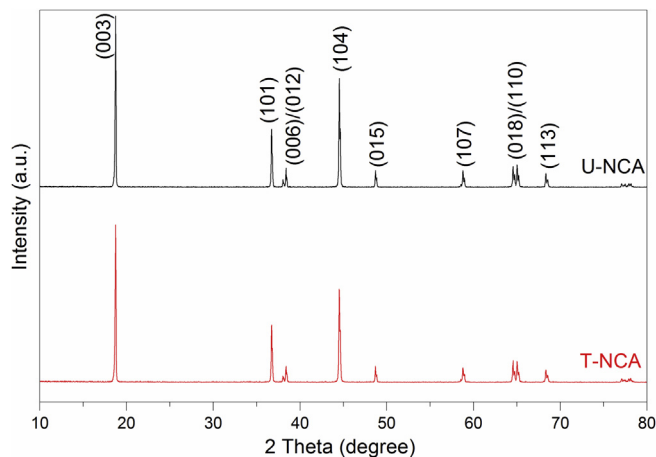

Fig. 1. XRD patterns of U-precursor and T-precursor.

Fig. 2. XRD patterns of U-NCA and T-NCA.

Table 1
Lattice parameters of T-NCA and U-NCA.

Sample	a (Å)	c (Å)	c/a	$I_{(003)}/I_{(104)}$
T-NCA	2.86698	14.18403	4.94	1.57
U-NCA	2.86680	14.18397	4.95	1.66

Fig. 5 shows the SEM images of T-precursor (Fig. 5a) and the corresponding T-NCA (Fig. 5d) samples, accompanied with the energy dispersive spectrometer (EDS) spectra (Fig. 5b and e) and the EDS elemental mappings for Mn (Fig. 5c and f). In Fig. 5a we can observe the smooth skin of the T-precursor particles with a diameter of about 10 μm. EDS spectra in Fig. 5b and e confirms the existence of Mn in T-precursor and T-NCA. Furthermore, the EDS elemental mappings, shown in Fig. 5c and f, exhibit the uniform distribution of Mn on their surfaces. To determine the distribution of Mn along the depth of a T-NCA particle, SEM and linear sweep EDS on a cross-section of the T-NCA sample were implemented, as shown in Fig. 6. Fig. 6a shows the cross-sectional SEM image of T-NCA. The white line is the scanning track and the red (in the web version) arrow, which is parallel with it, shows the scanning direction. The signals of Ni and Mn along the scanning track are plotted in Fig. 6b, which can indicate the relative amount of Ni and

Mn respectively. As seen in Fig. 6b, the concentration of Mn in the outer layer is significantly higher than that in the inner bulk. On the contrary, the concentration of Ni in the outer layer is reduced. It seems like that Ni and Mn distribute with concentration-gradient from surface to the depth of several hundred nanometers.

In order to clarify the amount of Mn in the T-NCA sample, we used ICP-OES to examine the chemical composition of T-UCA and U-NCA. The results of ICP are listed in Table 2, from which it can
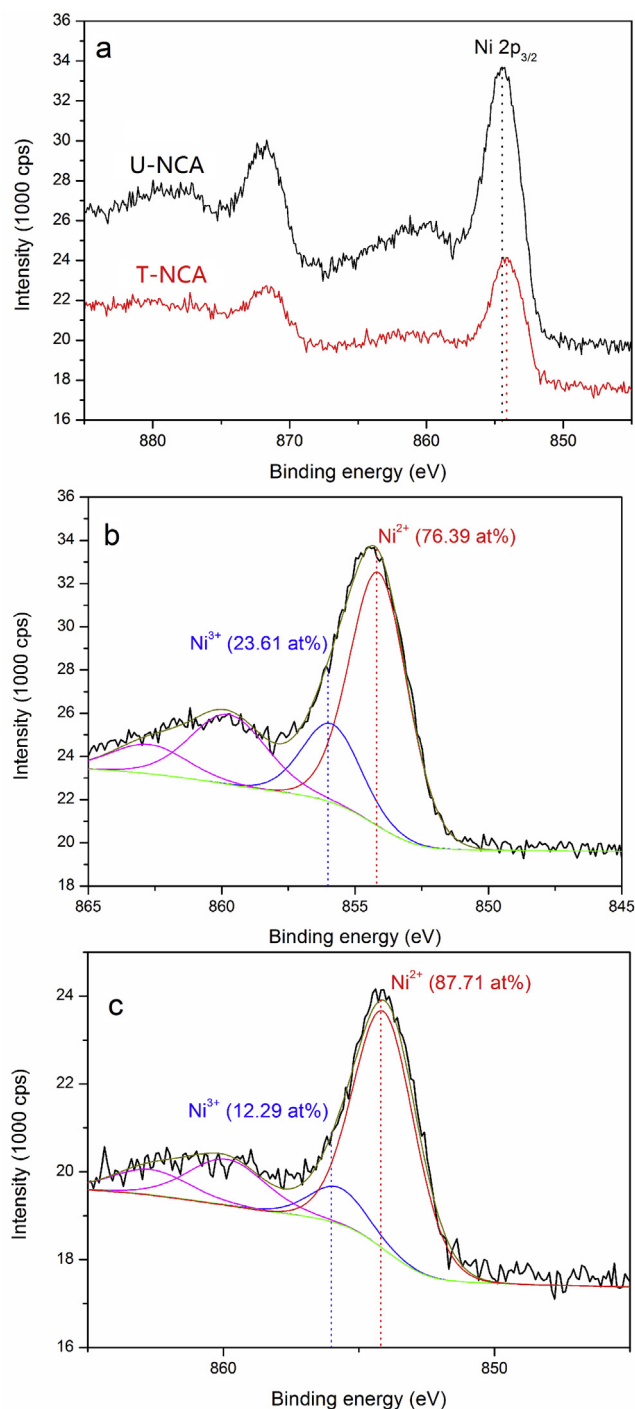

Fig. 4. XPS spectra of Ni(2p) for (a) U-NCA and T-NCA, and the magnified spectra of Ni $2p_{3/2}$ peaks for (b) U-NCA and (c) T-NCA.
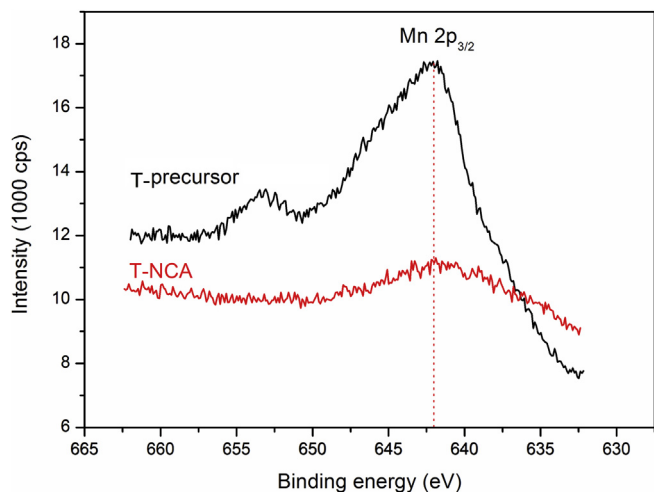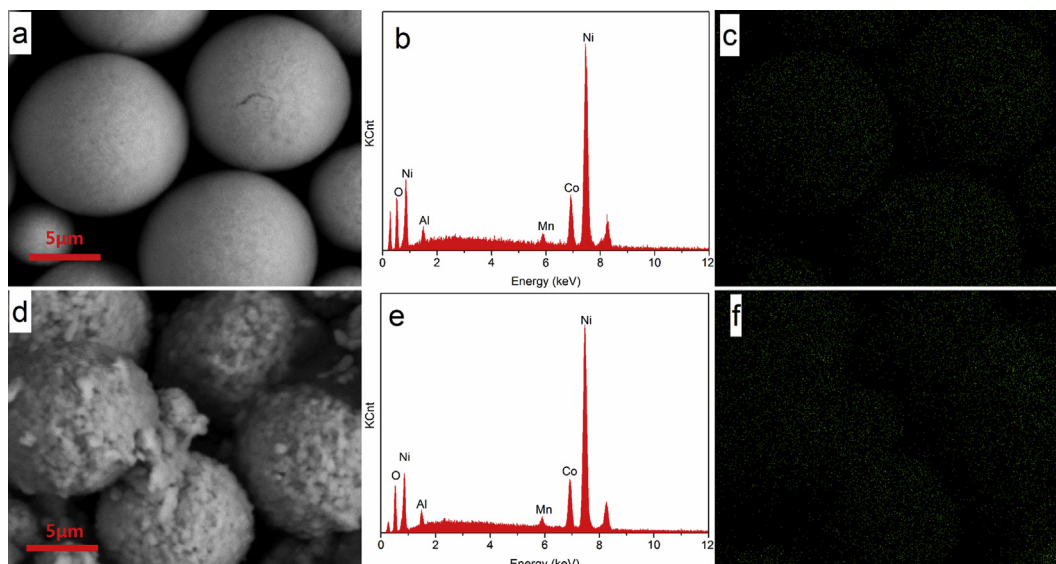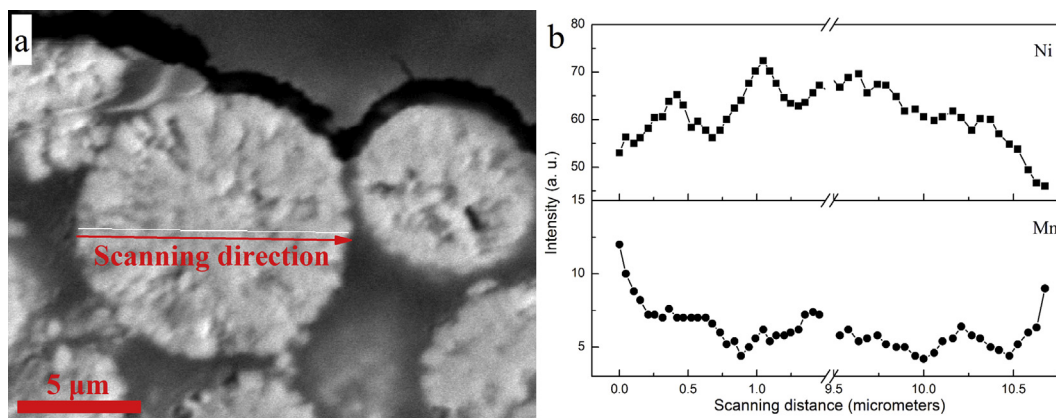

Fig. 3. XPS spectra of Mn(2p) for T-precursor and T-NCA.

Fig. 5. SEM images of (a) T-precursor and (d) T-NCA, the corresponding EDS spectra of (b) T-precursor and (e) T-NCA, and EDS mapping of Mn on (c) T-precursor and (f) T-NCA.

Fig. 6. (a) Cross-sectional SEM image of T-NCA and (b) the linear sweep EDS signals of Ni and Mn obtained from the cross-section of T-NCA particle.

be seen that the average chemical composition of T-NCA is $LiNi_{0.795}Co_{0.152}Al_{0.043}Mn_{0.010}O_2$.

3.2. Electrochemical characterizations

In this subsection, we will show a comprehensive contrastive research on electrochemical properties between T-NCA and U-NCA. Fig. 7a shows the initial charge–discharge curves at 0.1 C under room-temperature. It can be seen that the two samples exhibit almost the same initial discharge capacity of 189 mAh g^{-1}. However, their cycling performances (2 C), shown in Fig. 7b, show

Table 2
Element composition of T-NCA and U-NCA by ICP-OES.

Element	[Metal]/[Ni + Co + Al + Mn] (mol%)	
	U-NCA	T-NCA
Ni	80.15	79.47
Co	15.41	15.19
Al	4.44	4.30
Mn	0	1.04

obvious distinction. After 300 cycles, the discharge capacity of T-NCA is 106.6 mAh g^{-1}, which is remarkably higher than that of U-NCA (68.5 mAh g^{-1}). And the capacity retentions of T-NCA and U-NCA are 65.2% and 43.5% respectively. Fig. 7c presents the discharge capacities of T-NCA and U-NCA as a function of C rate (1 C corresponds to 200 mA g^{-1}) between 2.8 and 4.3 V under room temperature. The charging current is equal to the discharging current in every charge–discharge cycle. As can be seen that the discharge capacities of the two samples are nearly the same at 0.1 C rate, but the capacity loss of U-NCA is slightly larger than that of T-NCA at higher rates.
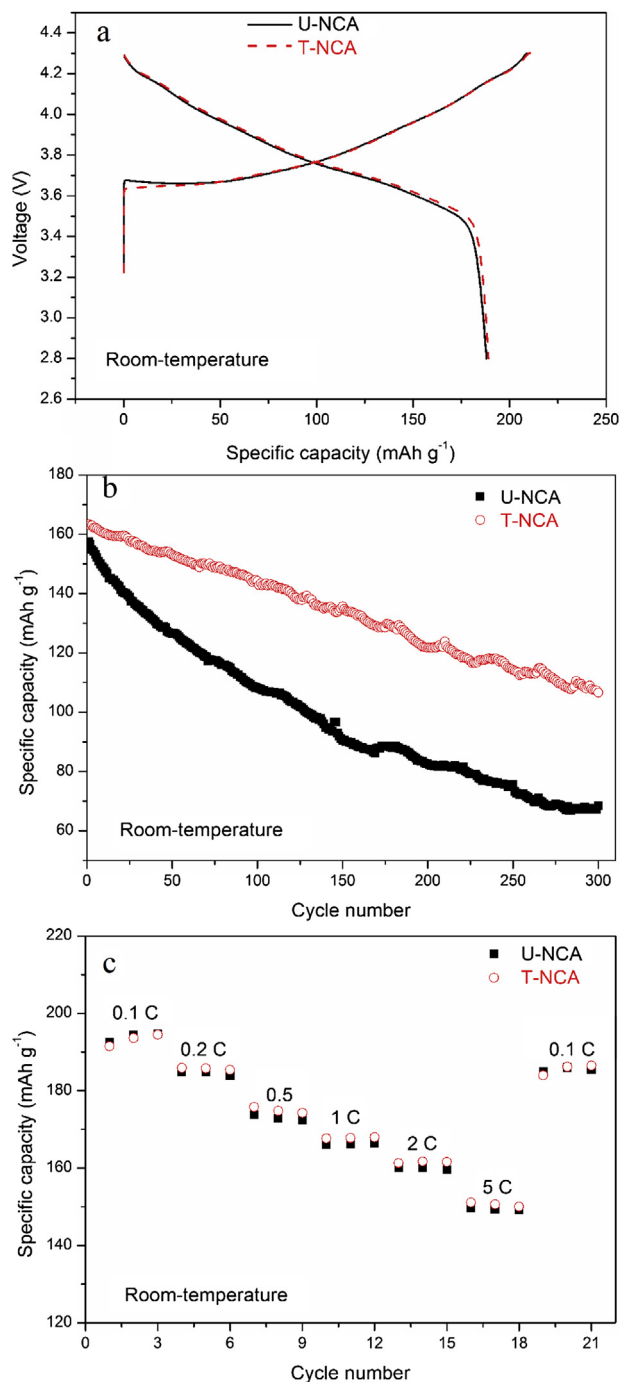
Fig. 8 shows the initial charge–discharge curves (0.1 C) and the cycling performances (2 C) of T-NCA and U-NCA at 55 °C. The initial charge–discharge curves, shown in Fig. 8a, almost fully overlap and illustrate the discharge capacity of 203 mAh g^{-1}. But as seen from Fig. 8b, the capacity fading of T-NCA, like the trend under room temperature, is significantly suppressed during charge–discharge cycles. We can see that the T-NCA sample delivers 115.9 mAh g^{-1} with a capacity retention of 67.5% after 100 cycles while U-NCA has only 84.4 mAh g^{-1} and its capacity retention is 49.3%.

Fig. 9a and b shows the initial charge–discharge curves (0.1 C) and the cycling performances (2 C) of T-NCA and U-NCA between

Fig. 7. (a) Initial charge–discharge curves of U-NCA and T-NCA at 0.1 C rate, (b) the cycling performances at 2 C rate and (c) their rate capabilities. All the tests were carried out from 2.8 to 4.3 V under room-temperature.

Fig. 8. (a) Initial charge–discharge curves of U-NCA and T-NCA at 0.1 C rate and (b) their cycling performances at 2 C rate. The tests were carried out from 2.8 to 4.3 V at 55 °C.

their cycling performances. We can see that T-NCA has a discharge capacity of 128 mAh g^{-1} after 100 cycles while U-NCA delivers 112.8 mAh g^{-1}. Their respective capacity retentions are 75.2% and 67.1%.

Grounded on the above results, it is reasonable to conclude that the Mn-surface-modified LiNi$_{0.8}$Co$_{0.15}$Al$_{0.05}$O$_2$ has slower capacity fading than the pristine one even under elevated temperature and overcharge condition. According to Cho et al.'s report [24], a small amount of Mn^{4+} (less than 10 mol %) on the surface of LiNiO$_2$-based materials is just as a dopant so that there only exist single phase of layered hexagonal structure. But because of the Mn^{4+} dopant, the surface Ni^{3+} ions tend to be reduced to Ni^{2+} ions and partly migrate to Li slab, forming a nanoscaled rock salt NiO phase which can act as a protective pillaring layer on the surface of the particles. Additionally, Noh et al. [25] reported that the presence of Mn^{4+} could stabilize the crystal structure by increasing the bond strength between Mn and O. Thus the structural stability could be enhanced by the tetravalent Mn in the surface region of the Ni-rich particles. Moreover, a Mn-rich outer layer can significantly reduce Ni content at particle surface (such as the famous concentration-gradient cathode [21,27]). The surface Ni^{2+} and Ni^{3+} will translate to Ni^{4+} at the end of charge, which is highly oxidative and readily oxidizes the electrolyte upon charge to high voltages. Coupling the previous physical and electrochemical characterizations we can infer that when Mn^{4+} dopes in the surface layer of the particles, a part of Ni^{3+} ions in the surface region are reduced to Ni^{2+} ions, leading to a higher degree of cation mixing and consequently fostering an
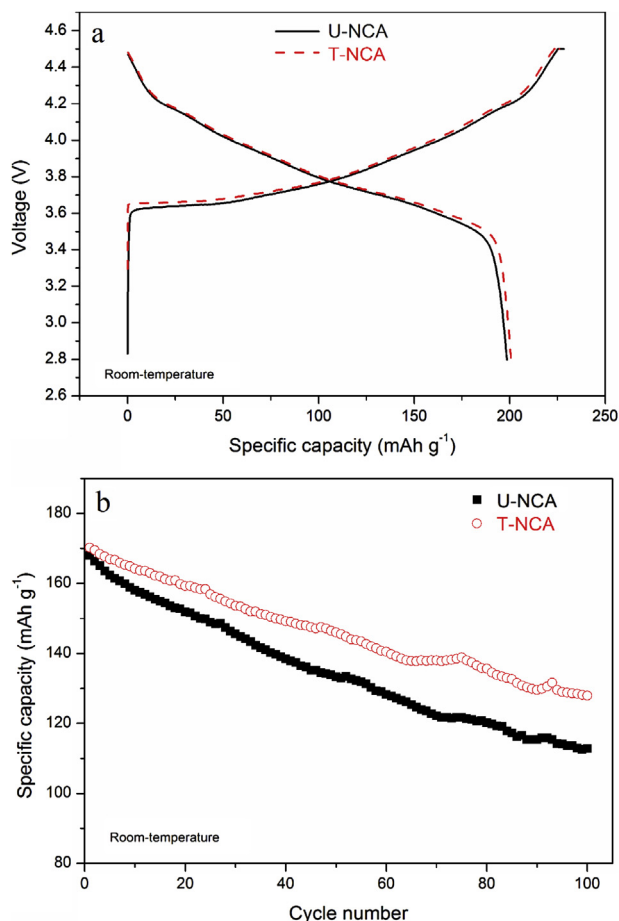
2.8 and 4.5 V for studying the overcharge behaviors. These tests were implemented under room temperature. As seen in Fig. 9a, T-NCA exhibits an initial discharge capacity of 200.7 mAh g^{-1} which is slightly higher than that of U-NCA (198.6 mAh g^{-1}). Considering the misalignment between the two charge–discharge curves, we calculated the initial coulombic efficiency of the two samples. The values of T-NCA and U-NCA are 88.8% and 86.9% respectively. This result encourages us to believe that the Mn containing surface can suppress the irreversible capacity loss under overcharge condition which may lead to the microstructural changes [9]. Fig. 9b shows

Fig. 9. (a) Initial charge–discharge curves of U-NCA and T-NCA at 0.1 C rate and (b) their cycling performances at 2 C rate. The tests were carried out from 2.8 to 4.5 V under room-temperature.
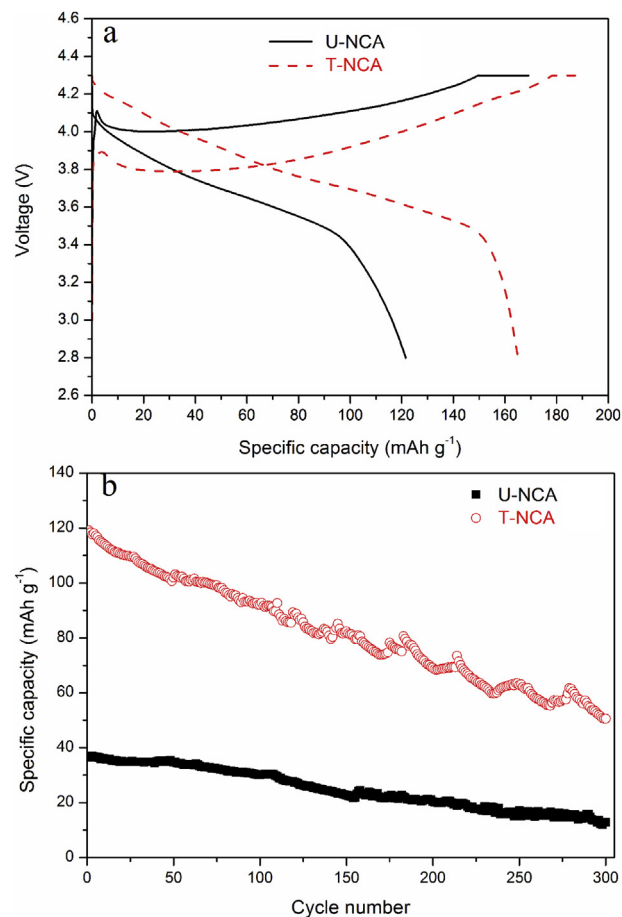

Fig. 10. (a) Initial charge–discharge curves of U-NCA and T-NCA at 0.1 C rate after storage in air for 50 days and (b) their cycling performances at 2 C rate. The tests were carried out from 2.8 to 4.3 V under room-temperature.

"artificial" protective NiO layer on the surface. This pillaring layer plays an important role in stabilizing the interface between the cathode and electrolyte. A stable solid-electrolyte interface (SEI) film can suppress the formation of unwanted resistive layers between the cathode and electrolyte, which gravely hinders the charge transfer kinetics [28–31]. This is the reason why the surface modification plays positive effects on the rate capability of the material. Moreover, the Mn-surface-modified material has reduced Ni content at particle surface and exhibits lower oxidizing ability. As a consequence, the Mn-surface-modified sample exhibits suppressed capacity fading, even under elevated temperature and higher cut-off voltage.

In addition to this, storage property of Ni-rich materials is also very important for their practical applications. According to literature [6,7,32–34], Ni-rich cathode materials degrade faster than low Ni-content materials upon exposure to air due to the spontaneous reduction of Ni^{3+} to Ni^{2+}. Thus, to further compare the degradation between T-NCA and U-NCA during storage, the electrochemical properties of the two samples after storage in air are investigated. Fig. 10a shows the initial charge–discharge curves of T-NCA and U-NCA at 0.1 C after storage in air for 50 days. The T-NCA sample has a discharge capacity of 165.0 mAh g^{-1} with a coulombic efficiency of 87.2%; however, U-NCA delivers a discharge capacity of 121.5 mAh g^{-1} only, and the coulombic efficiency is 71.8%. In addition, it can be observed that the discharge curve of U-NCA is wide apart from the charge part, indicating a large polarization. But

the polarization arising during storage in T-NCA is markedly suppressed. Fig. 10b shows the cycling performances of them at 2 C rate. The discharge capacities of T-NCA and U-NCA before cycles are 119.2 and 36.5 mAh g^{-1}; and after 300 cycles, the values are 50.6 and 12.9 mAh g^{-1} respectively. These results confirm that the
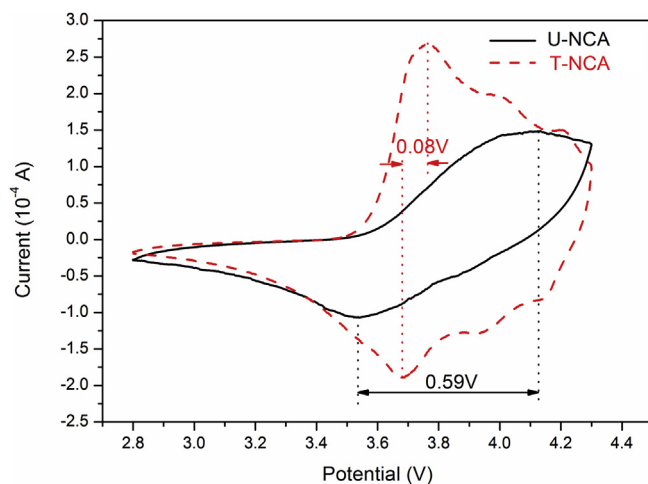
Fig. 11. Cyclic voltammograms obtained with scan rate of 0.1 mV s^{-1} for T-NCA and U-NCA after storage in air for 50 days.
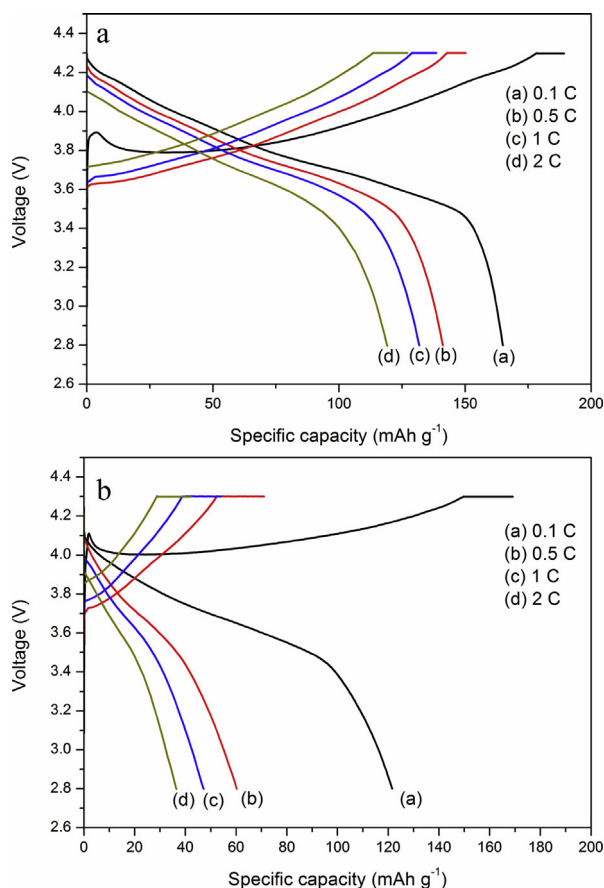
Fig. 12. The charge–discharge curves of (a) T-NCA and (b) U-NCA at various C rates after storage in air for 50 days.

presence of tetravalent Mn at the surface delays the degradation of $LiNi_{0.8}Co_{0.15}Al_{0.05}O_2$.

Cyclic voltammograms of T-NCA and U-NCA after storage in air for 50 days are shown in Fig. 11. The cells were tested at a scan rate of 0.1 mV s^{-1} between 2.8 and 4.3 V. Three peaks on both the oxidation and reduction curves of T-NCA can be observed, corresponding to the deintercalation/intercalation of Li$^+$ [35]. The potential difference between anodic and cathodic peaks is considered as the degree of polarization [36]. As can be seen in Fig. 11, the potential difference between the main anodic peak and main cathodic peak for T-NCA is 0.08 V. Contrastively, the value for U-NCA is 0.59 V, indicating a much larger polarization in the cell

Table 3
Lattice parameters of T-NCA and U-NCA after storage in air for 50 days.

Sample	a (Å)	c (Å)	c/a	$I_{(003)}/I_{(104)}$
T-NCA	2.86873	14.18437	4.94	1.16
U-NCA	2.87734	14.18447	4.93	1.00

assembled using U-NCA. This is consistent with the previous results.

Furthermore, the rate capabilities after storage are investigated. Fig. 12 presents the charge–discharge curves of T-NCA and U-NCA at various rates (0.1–2 C) between 2.8 and 4.3 V. Apparently, the T-NCA sample delivers higher discharge capacities than U-NCA at all the tested C rates, especially at high rates. For example, T-NCA exhibits a discharge capacity of 119.2 mAh g^{-1} at 2 C rate, whereas the U-NCA has only 36.5 mAh g^{-1} at the same current density.

Further evidence for the suppressing degradation in the T-NCA sample can be observed from XRD and XPS spectra of the two samples after storage in air (shown in Fig. 13). The lattice constants a and c are calculated based on the X-ray diffraction patterns (Fig. 13a) and listed in Table 3, together with the values of c/a and $I_{(003)}/I_{(104)}$. As indicated by Table 3, the lattice parameters a and c become larger (compared to the values in Table 1) after storing in air, which is in accord with Xiong's report [36]. And the values of c/a and $I_{(003)}/I_{(104)}$ become smaller compared to those of their fresh status, indicating that the degree of cation mixing gets higher in both the samples. However, it is worthwhile to note that the T-NCA sample has slightly larger c/a and $I_{(003)}/I_{(104)}$ values, showing a lower degree of cation mixing. Fig. 13b illustrates XPS spectra of Ni 2p$_{3/2}$ for T-NCA and U-NCA. It can be seen that the Ni 2p$_{3/2}$ peak of T-NCA is significantly higher than that of U-NCA, which reveals that the increment of Ni^{2+} species in U-NCA is more severe than in T-NCA. In other words, the T-NCA sample exhibits a slower reduction process of Ni^{3+} to Ni^{2+} which can be seen as the origin of deterioration for LiNiO$_2$ cathode [7].

4. Conclusions

We have successfully improved the electrochemical properties of $LiNi_{0.8}Co_{0.15}Al_{0.05}O_2$ via a facile in situ oxidizing-coating process. Based on XRD, SEM, EDS and EDS mapping analysis, we know that Mn^{4+} ions distribute uniformly on the surface of the material particles, and the concentration of Ni in the outer layer is reduced by the Mn-surface-modification. From the electrochemical characterizations, we confirm that the presence of tetravalent Mn at the surface can suppress the capacity fading during charge–discharge cycles under room temperature, elevated temperature and over-charge conditions. In addition, the tetravalent Mn also delays the
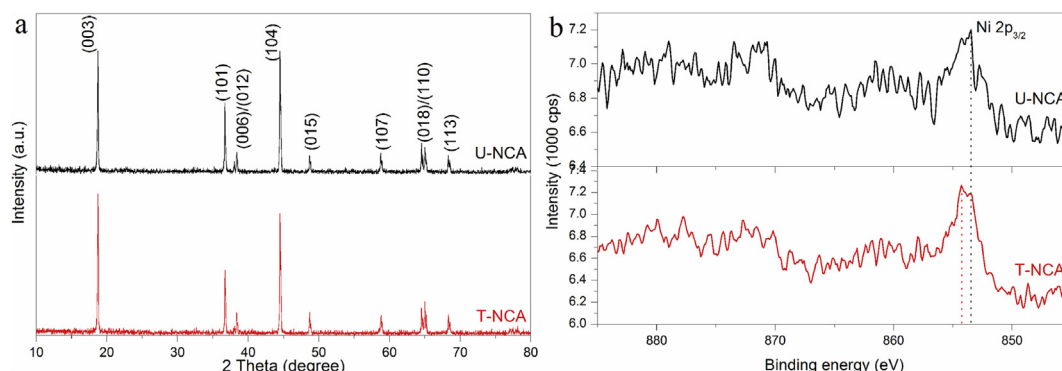

Fig. 13. (a) XRD patterns and (b) XPS spectra of T-NCA and U-NCA after storage in air for 50 days.

degradation during storage in air. Therefore, we consider this method as an effective way to stabilize the surface for other Ni-rich materials.

Acknowledgments

References

[1] D.-J. Lee, B. Scrosati, Y.-K. Sun, J. Power Sources 196 (2011) 7742—7746.
[2] D.P. Abraham, E.M. Reynolds, E. Sammann, A.N. Jansen, D.W. Dees, Electrochim. Acta 51 (2005) 502—510.
[3] W.-S. Yoon, K.Y. Chung, J. McBreen, X.-Q. Yang, Electrochem. Commun. 8 (2006) 1257—1262.
[4] T.-H. Kim, J.-S. Park, S.K. Chang, S. Choi, J.H. Ryu, H.-K. Song, Adv. Energy Mater. 2 (2012) 860—872.
[5] T. Nonaka, C. Okuda, Y. Seno, Y. Kondo, K. Koumoto, Y. Ukyo, J. Electrochem. Soc. 154 (2007) A353—A358.
[6] X. Xiong, Z. Wang, P. Yue, H. Guo, F. Wu, J. Wang, X. Li, J. Power Sources 222 (2013) 318—325.
[7] H.S. Liu, Z.R. Zhang, Z.L. Gong, Y. Yang, Electrochem. Solid-State Lett. 7 (2004) A190—A193.
[8] A.H. Tavakoli, H. Kondo, Y. Ukyo, A. Navrotsky, J. Electrochem. Soc. 160 (2013) A302—A305.
[9] S. Zheng, R. Huang, Y. Makimura, Y. Ukyo, C.A.J. Fisher, T. Hirayama, Y. Ikuhara, J. Electrochem. Soc. 158 (2011) A357—A362.
[10] J. Shim, R. Kostecki, T.J. Richardson, X. Song, K.A. Striebel, J. Power Sources 112 (2002) 222—230.
[11] D.P. Abraham, R.D. Twesten, M. Balasubramanian, I. Petrov, J. McBreen, K. Amine, Electrochem. Commun. 4 (2002) 620—625.
[12] Q. Liu, K. Du, H. Guo, Z.-d. Peng, Y.-b. Cao, G.-r. Hu, Electrochim. Acta 90 (2013) 350—357.
[13] S. Muto, K. Tatsumi, Y. Kojima, H. Oka, H. Kondo, K. Horibuchi, Y. Ukyo, J. Power Sources 205 (2012) 449—455.
[14] T. Sasaki, V. Godbole, Y. Takeuchi, Y. Ukyo, P. Novák, J. Electrochem. Soc. 158 (2011) A1214—A1219.
[15] Y.-R. Bak, Y. Chung, J.-H. Ju, M.-J. Hwang, Y. Lee, K.-S. Ryu, J. New Mat. Electrochem. Syst. 14 (2011) 203—207.
[16] Y.-M. Chung, S.-H. Ryu, J.-H. Ju, Y.-R. Bak, M.-J. Hwang, K.-W. Kim, K.-K. Cho, K.-S. Ryu, Bull. Korean Chem. Soc. 31 (2010) 2304—2308.
[17] Y. Cho, Y.-S. Lee, S.-A. Park, Y. Lee, J. Cho, Electrochim. Acta 56 (2010) 333—339.
[18] Y. Cho, J. Cho, J. Electrochem. Soc. 157 (2010) A625—A629.
[19] S.-W. Cho, G.-O. Kim, J.-H. Ju, J.-W. Oh, K.-S. Ryu, Mater. Res. Bull. 47 (2012) 2830—2833.
[20] Y. Cho, S. Lee, Y. Lee, T. Hong, J. Cho, Adv. Energy Mater. 1 (2011) 821—828.
[21] Y.-K. Sun, Z. Chen, H.-J. Noh, D.-J. Lee, H.-G. Jung, Y. Ren, S. Wang, C.S. Yoon, S.-T. Myung, K. Amine, Nat. Mater. 11 (2012) 942—947.
[22] Y.-K. Sun, B.-R. Lee, H.-J. Noh, H. Wu, S.-T. Myung, K. Amine, J. Mater. Chem. 21 (2011) 10108—10112.
[23] Y.-K. Sun, D.-H. Kim, C.S. Yoon, S.-T. Myung, J. Prakash, K. Amine, Adv. Funct. Mater. 20 (2010) 485—491.
[24] Y. Cho, P. Oh, J. Cho, Nano Lett. 13 (2013) 1145—1152.
[25] H.-J. Noh, S.-T. Myung, H.-G. Jung, H. Yashiro, K. Amine, Y.-K. Sun, Adv. Funct. Mater. 23 (2013) 1028—1036.
[26] G. Hu, W. Liu, Z. Peng, K. Du, Y. Cao, J. Power Sources 198 (2012) 258—263.
[27] Y.-K. Sun, S.-T. Myung, B.-C. Park, J. Prakash, I. Belharouak, K. Amine, Nat. Mater. 8 (2009) 320—324.
[28] J.M. Zheng, Z.R. Zhang, X.B. Wu, Z.X. Dong, Z. Zhu, Y. Yang, J. Electrochem. Soc. 155 (2008) A775—A782.
[29] Y. Wu, A. Manthiram, Electrochem. Solid-State Lett. 9 (2006) A221—A224.
[30] S.-U. Woo, C.S. Yoon, K. Amine, I. Belharouak, Y.-K. Sun, J. Electrochem. Soc. 154 (2007) A1005—A1009.
[31] Y.-K. Sun, S.-W. Cho, S.-W. Lee, C.S. Yoon, K. Amine, J. Electrochem. Soc. 154 (2007) A168—A172.
[32] J. Eom, M.G. Kim, J. Cho, J. Electrochem. Soc. 155 (2008) A239—A245.
[33] G.V. Zhuang, G. Chen, J. Shim, X. Song, P.N. Ross, T.J. Richardson, J. Power Sources 134 (2004) 293—297.
[34] K. Matsumoto, R. Kuzuo, K. Takeya, A. Yamanaka, J. Power Sources 81—82 (1999) 558—561.
[35] Y. Kojima, S. Muto, K. Tatsumi, H. Kondo, H. Oka, K. Horibuchi, Y. Ukyo, J. Power Sources 196 (2011) 7721—7727.
[36] X. Xiong, Z. Wang, G. Yan, H. Guo, X. Li, J. Power Sources 245 (2014) 183—193.